Three-dimensional image quality test phantom for planar X-ray imaging

AUTHORS:
John B. Noonoo[1]
Edem Sosu[1,2]
Francis Hasford[1,2]

AFFILIATIONS:
[1]School of Nuclear and Allied Sciences, University of Ghana, Accra, Ghana
[2]Radiological and Medical Sciences Research Institute, Ghana Atomic Energy Commission, Accra, Ghana

CORRESPONDENCE TO:
John Noonoo

EMAIL:
jbnoonoo@gmail.com

DATES:
Received: 05 July 2022
Revised: 14 Dec. 2022
Accepted: 12 Jan. 2023
Published: 08 Aug. 2023

HOW TO CITE:
Noonoo JB, Sosu E, Hasford F. Three-dimensional image quality test phantom for planar X-ray imaging. S Afr J Sci. 2023;119(7/8), Art. #14269. https://doi.org/10.17159/sajs.2023/14269

ARTICLE INCLUDES:
☒ Peer review
☐ Supplementary material

DATA AVAILABILITY:
☐ Open data set
☐ All data included
☒ On request from author(s)
☐ Not available
☐ Not applicable

EDITOR:
Michael Inggs

KEYWORDS:
3D printing, phantom, image quality, contrast, resolution

FUNDING:
None

We aimed to produce a simple, inexpensive 3D printed phantom as a prototype for image quality assessment of contrast, contrast-to-noise ratio (CNR), signal-to-noise ratio (SNR) and resolution in planar X-ray imaging systems. The test phantom was designed using SOLIDWORKS software, printed with a polylactic acid material and filled with paraffin wax. Circular aluminium sheets were used as inserts for contrast evaluation. A planar X-ray system was used for imaging and DICOM images were evaluated using ImageJ software. We evaluated spatial resolution, contrast, CNR and SNR. For resolution, full width at half maximum (FWHM) was measured on different grid sizes. For contrast, intensity of grey values and standard deviation were calculated on the different grid sizes. For CNR and SNR, difference in greyscale of investigated tissue and background per standard deviation of noise in the background was calculated. Resolution of the system was evaluated to be 1.57 and 1.80 lp/mm on grids A and B respectively. Contrast showed differential attenuation per variation in thickness. CNR increased from –13.7 for a thickness of 0.00 mm to 24.90 for a thickness of 28 mm. CNR did not change for a thickness greater than 16.0 mm. The SNR of the system fell in the acceptable range of ≥ 5. The results from the analyses performed indicate that the test phantom has great potential to be a good substitute for the commercially available phantoms on the market, especially for low-resource settings.

Significance:

This study highlights the emergence of 3D printing technology and its suitability within radiology and medical physics for the production of cost-effective phantoms which can serve as substitutes for commercial phantoms in low-resourced medical facilities in low- and middle-income countries.

Introduction

Image quality assessment as a component of quality control in radiology departments is one of the many job descriptions of the clinical physicist. A variety of modality-specific phantoms are used in quality assurance examinations. However, these phantoms are expensive and sometimes delicate, and expert technicians are needed for their use and to evaluate their data.[1,2] Typically, commercially available phantoms are in the price range of USD4000 to USD10 000, depending upon the specifications and the applicable imaging modality.

Since its introduction in the 1980s, three-dimensional (3D) printing technology has progressed from its use in research facilities to being a widely used method for the construction of phantoms for use in diagnostics and radiotherapy.[3-5] Besides the printer technology, attempts have been made to synthesise materials that can be utilised to create 3D models such as resins. The printing process and material determine the quality of the printed product. 3D printing has recently been utilised to create phantoms for multimodality and modality-specific imaging.[6]

According to Huda and Abrahams[7], image quality in radiological imaging is determined by factors such as contrast, spatial resolution, signal-to-noise ratio and noise. Contrast[5] is defined as the difference between the mean greyscale in a region of interest in a study material (S_t) and the mean greyscale in a background area of interest (S_b). This is commonly referred to as the contrast-to-noise ratio (CNR) in digital imaging. In the presence of noise, it is an object-size-independent estimate of the signal strength in the study tissue. This is represented as[8]:

$$CNR = \frac{S_t - S_b}{\sigma_b} \qquad \text{Equation 1}$$

where σ_b is defined as the greyscale standard deviation of the noise in the background.

Spatial resolution is described[9] as the capacity of an imaging modality to distinguish two neighbouring structures as distinct from one another, i.e. image detail visibility. The resolution is mostly estimated using the full-width-at-half-maximum (FWHM) measure in units of line pairs per millimetre (lp/mm).

Signal-to-noise ratio is a measure of true signal (real anatomy) to noise. A lower SNR normally results in images with a gritty appearance. In radiology, SNR is proportional to the amount of contrast in the square root of transmitted photons.[10]

Noise is an undesirable feature in images as it obstructs visualisation and comprehension of an anomaly of interest.[11] The two most prevalent sources of noise in medical images are anatomical noise and radiographic noise. Anatomical noise is the term for undesirable anatomical anomalies in an image. As a result, anatomical noise characterisation is task dependent and independent of the inherent performance of a detector. Radiographic noise describes unwanted image variations that are not produced by the image subject.

A good quality control program can be used to evaluate the clinical performance of imaging systems. The outcomes of routine image quality control are compared to those acquired during equipment acceptance testing or to predefined baseline values at regular intervals. Differences in image quality are indicated by deviations from the acceptance test or baseline values. Periodic quality control helps to discover departures from optimal efficiency and lays the groundwork for continual development by providing frequent feedback. This might be beneficial to patient diagnosis and therapy.[12]

Three-dimensional (3D) printing has gained prominence in recent times for building volumetric objects with the help of a computer-aided design application and the use of a wide range of materials such as ceramics, resins, metals and thermoplastics (e.g. acrylonitrile butadiene styrene (ABS), polyethylene terephthalate glycol-modified (PETG) and polylactic acid (PLA)).[13] 3D printing in radiology has been used predominantly in the construction of phantoms for diagnostic radiology, nuclear medicine and radiotherapy. It has also been used in the printing of breast phantoms using materials as tissue substitutes for their attenuation coefficients.[14,15] Simple symmetrical phantoms for use in computerised tomography (CT) have been manufactured through 3D printing using tissue equivalent materials like resins and thermoplastics.[16] Anthropomorphic phantoms depicting the whole body[17] as well as body parts such as the spine[18] and head[19] have all been manufactured and are playing a key role in radiology departments worldwide.

Studies have been done on the manufacture of 3D-printed image quality assessment phantoms suitable for conventional X-ray imaging, mammography and fluoroscopy. One study[6] used PLA material to print a low-contrast phantom with air holes of different radii ranging from 0.5 mm to 4.5 mm and irradiated with a fluoroscopy machine of 40 kV – 70 kV and the results were feasible. The manufacture of a universal image quality phantom for use in general X-ray, mammography, CT and fluoroscopy has been explored.[2]

Three relevant issues are prevalent in image quality assessment in resource-limited facilities: the high cost of commercial phantoms, lack of human resources, and time constraints, with cost being chief among them. In this study, we therefore aimed to use 3D printing technology to develop an in-house image quality assessment phantom for resolution, contrast, contrast-to-noise ratio and signal-to-noise ratio for general X-ray imaging systems of a low-resourced centre in a low- to middle-income country (LMIC).

Materials and methods

Materials

SOLIDWORKS® software (Version 2019, Dassault Systemes, France) was used for the design of the test phantom. The Creality Slicer software (V.4.8.2 build 177 win 64, Shenzhen Creality 3D Technology Co., Limited, China) was used for G-code conversion of the SOLIDWORKS design to STL files and a Creality CR-20 Pro 3D Printer (Shenzhen Creality 3D Technology Co., Limited, China) was used to print the PLA material (density = 1.250 g/cm^3) into the 3D test phantom.

The PLA material is composed of hydrogen (0.058), carbon (0.541), nitrogen (0.018) and oxygen (0.383). It has a specific density of 1.43 g/cm^3, tensile strength of 28.8 MPa, bending strength of 58.6 MPa and a Hounsfield unit of -530 ± 25. It has linear attenuation coefficients of 0.439, 0.286 and 0.244 at kiloelectron volts of 30, 45 and 60 keV, respectively.[13,14]

The 3D-printed phantom was filled with paraffin wax, and aluminium sheets of 99% purity were inserted into the wax. Image quality assessment, using the phantom, was done on the Philips DuraDiagnost Release 4 X-ray machine (Koninklijke Philips N.V, Netherlands).

ImageJ software (Version 1.51, US National Institutes of Health and the Laboratory for Optical and Computational Instrumentation (LOCI, University of Wisconsin), USA) was used for image analysis. A tape measure, the Ocean software, Piranha quality control meter, the collimator and beam alignment quality control test tool and a beam alignment phantom were used for quality control procedures.

Phantom design and modelling

A circular-shaped phantom was designed, with a whole-body diameter of 150 mm, radius of 75 mm, and thickness of 45 mm and with eight circular holes on the surface (Figure 1). The holes were arranged in a coordinated orientation with equal tolerance in between them for accuracy in alignment. This arrangement was relevant for the measurement of contrast. Opposite the circular holes was a group of four squares of equal dimensions (27 mm × 27 mm) with gridlines of varied spacing in decreasing order of visibility, which is relevant for resolution. The design was saved in the STL format, a universally accepted format for computer-aided designs. ISO/ASTM 52900:2015 was used for the design and fabrication process.

3D printing

The fused deposition modelling method was used for printing the thermoplastic material. Printing of the phantom was done using different parameters. The axial setup was in the order of x-50, y-130 and z-9.99.

The temperature of the printer's nozzle remained constant at 240 °C. Printing time ranged from 1 h to 18 h for the different components of the phantom. A constant bed temperature of 60 °C was maintained throughout the printing process. The fan embedded in the printer, which primarily is used for cooling, was maintained at 50% of its capacity throughout the printing process.

Extruder filling

Paraffin wax was used as the filling material for the printed 'image quality' phantom (Figure 2). Paraffin wax was chosen for its high density and similarity to human tissue by properties. Paraffin wax candles were heated to 80 °C, allowed to cool and poured into the printer extruder (phantom) while in a semi-liquid state to fill in the empty spaces evenly without air gaps. The phantom was left in the open for up to 2 h to solidify and evenly fill every space. The finished test phantom had the specifications shown in Table 1.

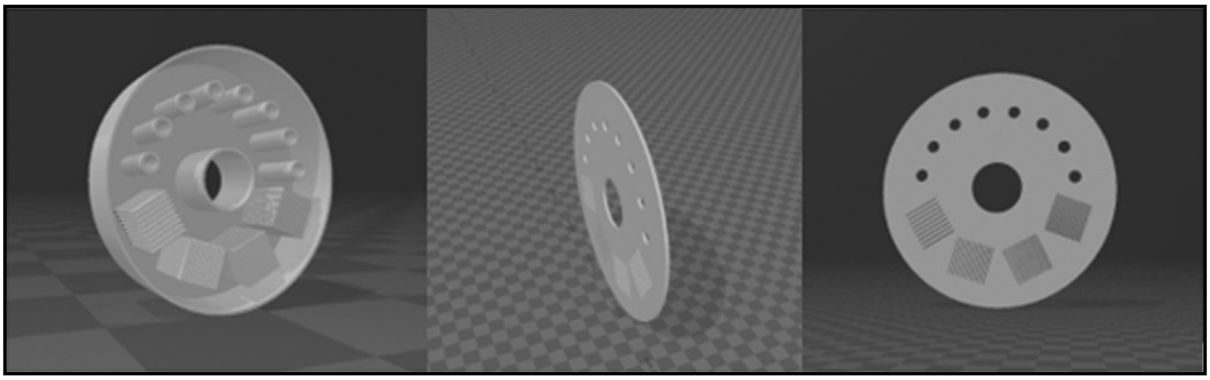

Figure 1: The eight-hole design concept and animation done with SOLIDWORKS.

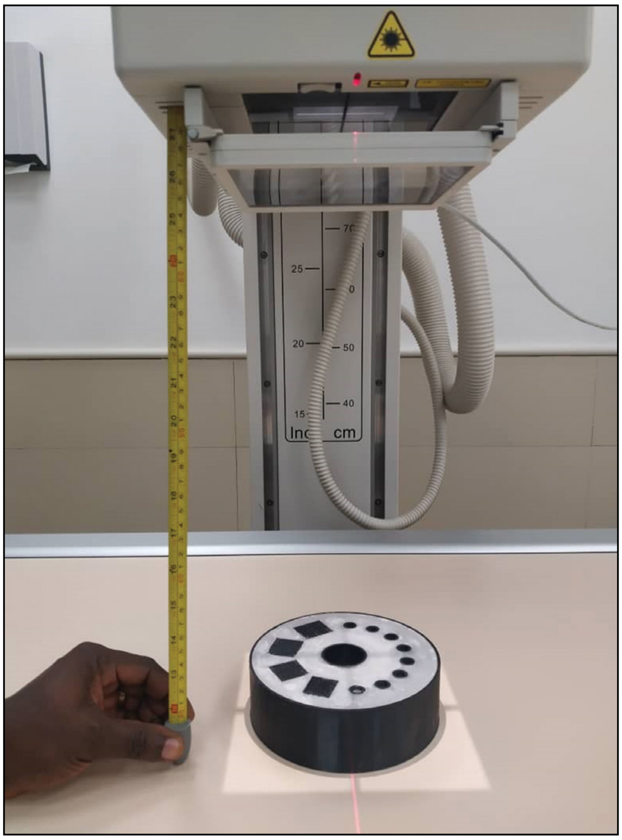

Figure 2: The 3D-printed phantom fully filled with paraffin wax and evenly set up for exposure with a conventional X-ray machine.

Table 1: Specifications and related dimensions of the test phantom

Specification	Dimensions (mm)
Phantom radius (R)	75
Phantom thickness (t)	45
Radius of circular holes (r)	5
Tolerance between circular holes (T_r)	8
Radius of aluminium discs	3.5
Thickness of aluminium discs	0.8
Spacing of resolution lines/bars	0.8/1.0/1.2/1.4
Radius of aluminium rod	4
Thickness of aluminium rod	45–10 (factor of 5)
Contrast squares	27 × 27

Exposure and acquisition of DICOM image

Images for the image quality assessment were acquired using the setup depicted in Figure 2. The circular holes on the phantom were filled with aluminium discs of diameter 7 mm. The discs, of 0.8 mm thickness, were placed on top of each other to form varying thicknesses in seven of the eight holes, with the first hole unfilled.

The phantom was set up on the couch of the X-ray machine just beneath the source. The distance between the source and the phantom was 700 mm. The X-ray source was set to 52 kVp, 63.0 ms and 32 mAs with 1.35 μGym^2.

DICOM (Digital Imaging and Communications in Medicine) is the primary file format for storing and transferring medical images.The DICOM image acquired (Figure 3) was uploaded to the ImageJ software and analysed using the various image quality assessment tools.[4] The acquired X-ray showed fine and clear details with minimal or no noise or artefacts.

Resolution

Analysis of resolution was done by drawing regions of interest across the gridlines. A polynomial fit of distance versus greyscale values was performed for each gridline. For each grid, the FWHM representing the resolution of the X-ray system was determined. The average resolution of each grid was calculated using Equation 2:

$$\text{Grid X, Line Y}$$

$$\text{Resolution peak} = \frac{\text{Highest curve peak}}{2} \qquad \text{Equation 2}$$

$$\text{Resolution} = \text{Highest value on xaxis} \\ - \text{Lowest value on x} - \text{axis}\ldots.$$

Contrast

Contrast was analysed by drawing regions of interest in the phantom image. Each of the holes in the image represented a different thickness and contrast due to the difference in the number of aluminium discs. Each thickness corresponded to the position of the circular hole in increasing order of contrast. A polynomial graph of thickness against mean greyscale value was plotted to show the curvature of contrast.

Contrast-to-noise ratio

Noise was determined by using the contrast-to-noise ratio (CNR). The standard deviation of the mean greyscale values was calculated. For each hole and thickness, the average greyscale in the region of interest (ROI) in the hole was found as well as the average greyscale in the ROI in the surrounding background. These two parameters were used to find the CNR together with the standard deviation of the noise in the background.

Signal-to-noise ratio

The SNR was estimated using Equation 3. For each thickness, the mean grey value in the ROI was found. The standard deviation of the mean

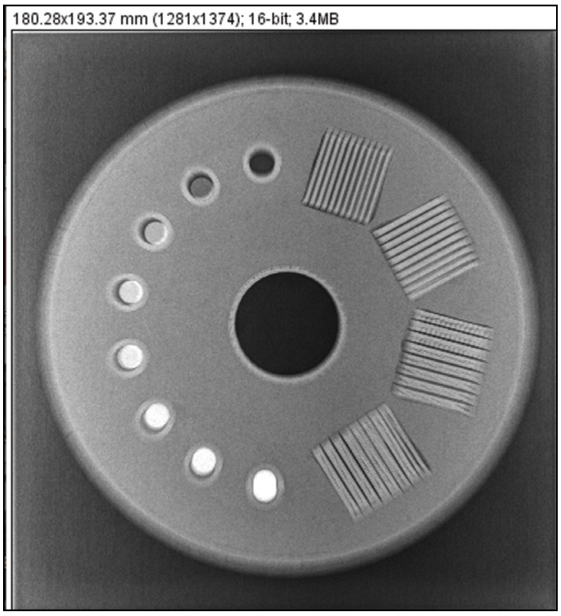

Figure 3: DICOM image of the phantom for image quality assessment.

grey values within the ROI was calculated. These two parameters were used to find the SNR.

$$\mathrm{SNR} = \frac{\text{Mean grey value within ROI}}{\text{Standard deviation of grey value within ROI}} \qquad \text{Equation 3}$$

Estimation of covariance (CoV) of the measured grey values gives a good insight into what is happening with the increase in thickness and was calculated as:

$$\mathrm{CoV} = \frac{\text{standard deviation of grey values}}{\text{mean grey values}} \times 100\%.... \qquad \text{Equation 4}$$

Results and discussion

Resolution

The spatial resolution of the planar X-ray system was determined from the gridlines of the phantom. The phantom consisted of four grids: A, B, C and D. The width of the lines/bars and their spacing for each grid were 0.8 mm, 1.0 mm, 1.2 mm and 1.4 mm, respectively. The ImageJ program evaluated the resolution by means of a data set collected in the parameters of distance and greyscale values. A polynomial graph of distance versus greyscale value was plotted for each line of every grid. Image resolution was evaluated quantitatively.

Table 2 shows the accumulation of the distance and initial and final grey values of Grids A and B. The distance and grey values for each line of the grids were generated from the ImageJ software. The final grey value is calculated by subtracting the initial grey value from the minimum value. This was done for all lines of Grids A and B.

Spatial resolution of the planar X-ray scanner was determined by calculating the full width at half maximum (FWHM) from each of the graphs in Figure 4. The FWHM was calculated using Equation 5.

$$\mathrm{FWHM} = |z_1 - z_2| \qquad \text{Equation 5}$$

where z_1 is the minimum distance (mm) value corresponding to the minimum grey value at $1/2h_{\max}$ and z_2 is the maximum distance (mm) value corresponding to the maximum grey value at $1/2h_{\max}$. Subtracting the minimum value of distance from the maximum value gives the resolution value for the grid and line under consideration.

Table 3 shows the spatial resolution measured from the three lines for Grids A and B. It can be observed that the grey value increases constantly with a corresponding increase in distance until it peaks and decreases steadily from the point of the highest peak as it approaches zero.

From Table 3, it can be seen that the average spatial resolution decreases with decreasing spatial frequency. The spatial frequency of Grid A (Table 2) produced an average FWHM of 1.57 mm, while the spatial frequency of Grid B (i.e. 1.0 mm width and 1.0 mm spacing) produced an average

Table 2: Cumulative table of distance and initial and final pixel grey values for Grids A and B

Distance (mm)	**Grey value (initial)**						**Grey value (final)**					
GAL1 – GBL3	**GAL1**	**GAL2**	**GAL3**	**GBL1**	**GBL2**	**GBL3**	**GAL1**	**GAL2**	**GAL3**	**GBL1**	**GBL2**	**GBL3**
0.0	1304.3	1033.2	1429.8	901.0	1028.0	2061.0	360.1	88.2	106.1	18.0	0.0	86.0
0.1	1107.5	945.0	1486.1	1117.3	1616.9	2138.6	163.3	0.0	162.4	234.3	588.9	163.6
0.3	1115.4	988.5	1436.8	2016.8	2431.4	2009.2	171.2	43.5	1131.0	1133.8	1403.4	34.2
0.4	1268.9	1146.1	1551.0	2496.5	2682.5	2147.8	324.7	201.1	227.3	1613.5	1654.5	172.8
0.6	1529.2	1498.3	1792.7	2491.9	2660.0	2470.3	585.0	553.3	469.0	1608.9	1632.0	495.3
0.7	2056.8	1959.4	2129.8	2418.5	2690.2	2677.1	1112.6	1014.4	806.1	1535.5	1662.2	702.1
0.8	2425.4	2174.7	2592.1	2543.3	2848.3	2795.0	1481.2	1229.7	1268.4	1660.3	1820.3	820.0
1.0	2604.2	2538.4	2665.9	2742.1	2881.9	2775.2	1660.0	1593.4	1342.2	1859.1	1853.9	800.2
1.1	2652.4	2534.0	2648.1	2813.6	2761.9	2832.4	1708.2	1589.0	1324.4	1930.6	1733.9	857.4
1.3	2701.8	2623.3	2660.5	2850.0	2670.5	2858.0	1757.6	1678.3	1336.8	1967.0	1642.5	883.0
1.4	2509.6	2612.4	2523.2	2802.0	2770.2	2770.7	1565.4	1667.4	1199.5	1919.0	1742.2	795.7
1.5	2552.0	2553.5	2112.5	2755.4	2694.1	2910.4	1607.8	1608.5	788.8	1872.4	1666.1	935.4
1.7	2362.0	2078.9	1731.5	2375.3	2528.0	2804.0	1417.8	1133.9	407.8	1492.3	1500.0	829.0
1.8	1940.0	1577.3	1388.4	2247.7	2386.3	2455.8	995.8	632.3	64.7	1364.7	1358.3	480.8
2.0	1376.4	1248.5	1323.7	2288.6	2265.1	2182.7	432.2	303.5	0.0	1405.6	1237.1	207.7
2.1	1024.6	1102.9	1387.6	2155.0	1977.5	1978.8	80.4	157.9	63.9	1272.0	949.5	3.8
2.3	944.2	1016.4	1449.6	1585.6	1396.9	1975.3	0.0	71.4	125.9	702.6	368.9	0.3
2.4	1044.5	1068.9	1328.5	1033.9	1035.3	2175.8	100.3	123.9	4.8	150.9	7.3	200.8
2.5	1249.4	1149.4	1570.1	883.0	1030.0	2427.0	305.2	204.4	246.4	0.0	2.0	452.0
Min value	**944.2**	**945.0**	**1323.7**	**883.0**	**1028.0**	**1975.3**						

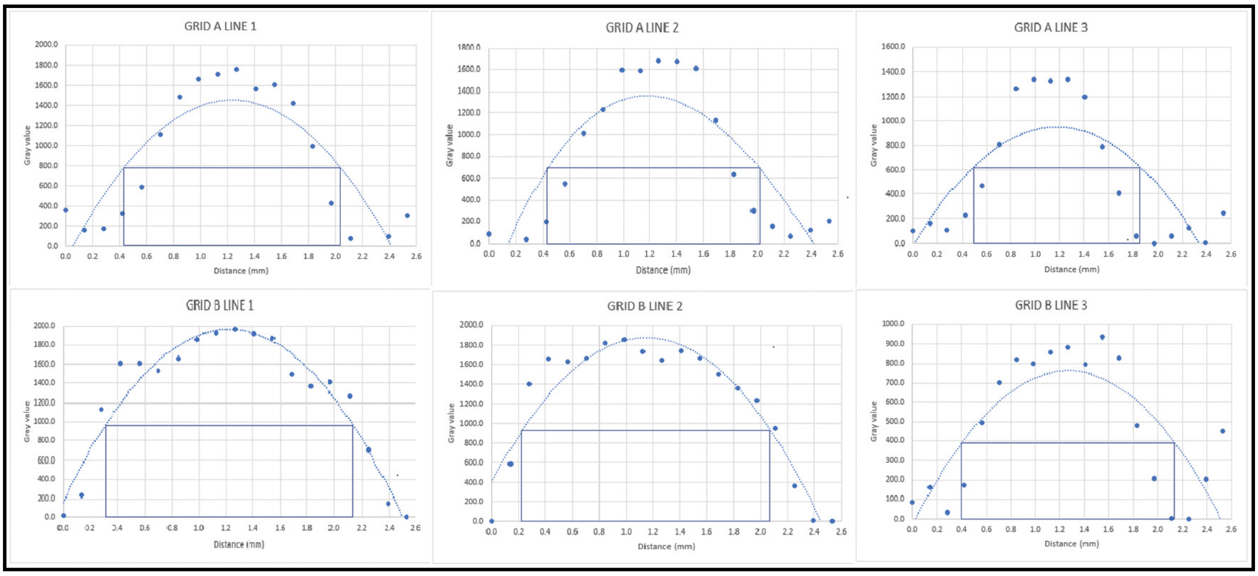

Figure 4: Resolution graphs for lines 1, 2 and 3 for Grids A and B.

Table 3: Resolution for lines of Grids A and B

GRID	Line 1			Line 2			Line 3			Average of differences
	Max	Min	Diff	Max	Min	Diff	Max	Min	Diff	
A	2.06	0.40	1.66	2.02	0.42	1.60	1.90	0.45	1.45	1.57
B	2.12	0.32	1.80	2.08	0.22	1.86	2.14	0.40	1.74	1.80

FWHM of 1.80 mm. This means that Grid A could be used to resolve lines/bars that are 1.57 mm wide with 1.57 mm spacing, while Grid B can be used to resolve lines/bars that are 1.80 mm wide with 1.80 mm spacing. The smaller the FWHM, the better the spatial resolution. Due to the difficulty in the 3D printing of Grid C (i.e. 1.2 mm width and 1.2 mm spacing) and Grid D (i.e. 1.4 mm width and 1.4 mm spacing), images of Grid C and D were not included for calculating the spatial resolution. As the resolution of Grid A is lower than those of Grid B, Grid C and Grid D, it was more efficient in resolving structures with sizes less than 1.80 mm.

Resolution of the phantom could be attributed to the type of material used for measuring the spatial resolution or exposure parameters, such as the source to image (phantom) distance, output voltage, tube current, and exposure time used in the acquisition of images. When the source to image distance increases, the X-ray beam diverges, forming a cone shape and thereby affecting the intensity of the X-ray beam and quantity of X-rays. Also, attenuation due to low kilovoltage peak may lead to the desired image not generating.

In this study, the FWHM was calculated based on the slit (i.e. grids) method on the digital detector. The resultant penumbral image provided a line spread function or Gaussian curve, from which the FWHM was estimated, due to a partial block of the radiation from the source by the grids.[20,21]

Contrast

Contrast was measured from eight holes of the same diameter and radius (Figure 3), filled with different thicknesses of aluminium inserts. Using the elliptical measurement tool in the Radiant DICOM viewer, an area of 0.1289 cm^2 was drawn in the centre of each circular image (i.e. as region of interest) to obtain the intensity of grey values and their standard deviation. The thickness of the target increased with greyscale values, but greyscale values remained fairly the same beyond a target thickness of 16 mm. There is an attainment of saturation in grey value for an aluminium thickness beyond 16 mm. Also, the CoV became better with an increase in thickness saturating from $\geq$ 20.0 mm. A CoV of $\leq$5% is normally acceptable and $\leq$10% is within a good range. Data from this analysis are presented in Table 4 and Figure 5.

The X-ray intensity attenuation across the material is approximately the same for thicknesses greater or equal to 16 mm. This implies that the maximum contrast that can be measured by the phantom using exposure parameters of 52 kVp, 32 mA, 63 ms and a source to phantom distance of 700 mm is 4095 at a phantom thickness greater or equal to 16 mm. This indicates the attainment of a saturation point for the mean grey values.

Contrast-to-noise ratio

The CNRs for each of the eight circular targets (holes) were also calculated using Equation 1.[8]

Table 5 shows the average greyscale in the ROI in the investigated tissues, backgrounds and standard deviations.

Negative CNR values indicate less signal than noise, and positive CNR values indicate more activation signal than noise.[22]

From Figure 5b, there is a steady increase in the CNR per aluminium thickness. This is because an increase in the depth of aluminium discs increases the relative X-ray transmittance in the phantom. The CNR increased from a negative value of –13.7 for a thickness of 0.00 mm to 24.90 for a thickness of 28.00 mm. In the exposure of the phantom for assessment, the first hole was left empty (without any aluminium insert) and this accounted for the 0.00 cm thickness. This is because without any aluminium insert present, there is no attenuation of X-rays in the medium, indicating less signal than noise. The CNR steadily increased per increase in thickness because attenuation increased as aluminium thickness increased. However, the CNR did not change considerably with an increase in thickness from 16 mm to 28 mm. The standard deviation within this range also showed a steady change, indicative of the attainment of a saturation point.

Table 4: Position of holes and their corresponding thicknesses, pixel grey values and signal-to-noise (SNR) ratios

Position	Thickness (mm)	Min grey value	Max grey value	Mean grey value	Standard deviation	SNR	Covariance (%)
1	0.0	618	976	815.44	61.93	13.17	7.6
2	4.0	1393	2019	1744.7	102.65	16.99	5.9
3	8.0	2638	3229	2892.29	99.01	100.26	3.4
4	12.0	3104	3835	3485.29	114.48	30.44	3.3
5	16.0	3431	4095	3793.71	113.39	33.46	3.0
6	20.0	3713	4095	4018.94	85.80	46.84	2.1
7	24.0	3719	4095	4009.25	86.95	46.11	2.1
8	28.0	4039	4095	4064.00	84.97	47.83	2.1

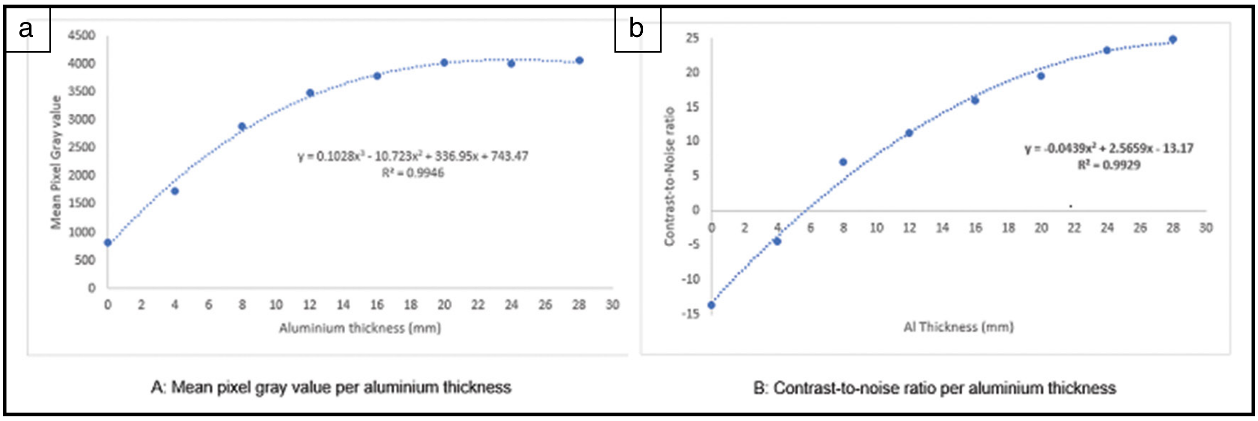

A: Mean pixel gray value per aluminium thickness

B: Contrast-to-noise ratio per aluminium thickness

Figure 5: (a) Mean pixel grey value per aluminium thickness and (b) contrast-to-noise ratio per aluminium thickness.

Table 5: Thickness, mean grey pixel values of the region of interest (ROI) in investigated tissue and background, with associated standard deviations and contrast-to-noise ratios (CNR)

Position	Thickness (mm)	Mean grey value in ROI in investigated tissue	Mean grey value in ROI in background	Standard deviation of background	CNR
1	0.0	815.44	2084.17	92.88	−13.66
2	4.0	1744.7	2153.48	94.22	−4.34
3	8.0	2893.29	2199.22	98.48	7.05
4	12.0	3485.39	2276.26	107.63	11.23
5	16.0	3793.71	2240.47	97.51	15.93
6	20.0	4018.94	2145.87	96.05	19.50
7	24.0	4009.25	1994.34	86.96	23.17
8	28.0	4064.00	1849.41	88.91	24.91

Signal-to-noise ratio

The signal-to-noise ratio (SNR) for each of the eight circular targets (holes) was calculated using Equation 3[22] as shown in Table 4. The SNR as a measure compares a desired signal to the level of background noise. The higher the CNR is between structures, the lower the SNR needed. From Figure 5b, there is a steady increase in the CNR per aluminium thickness, hence a higher SNR is required for differentiation. The SNR changed steadily from a thickness of 20 mm to 28 mm. The standard deviation within this range also showed a steady change, indicative of the attainment of a saturation point. According to the Rose model, the image quality of a system is acceptable if the SNR is greater or equal to 5.[23]

Conclusion

This study has shown that 3D printing techniques can be used for the manufacture of test phantoms for image quality assessment in planar X-ray imaging. We successfully designed and printed a test phantom for in-house use in a low-resourced medical imaging facility in a LMIC that assessed image quality successfully. The phantom demonstrated the capability of being used for analysing image quality parameters, including resolution, contrast and CNR on general X-ray imaging systems. Subsequent plans include acceptance testing and commissioning tests for clinical use. This in-house quality control equipment, at a unit price of USD150, could be a good substitute for relatively expensive commercially available phantoms.

Acknowledgements

This research was carried out at the Medical Physics Department of the School of Nuclear and Allied Sciences in the University of Ghana as part of the master's degree of J.B.N. The authors are grateful to the department for its support.

Competing interests

We have no competing interests to declare.

Authors' contributions

J.B.N.: Conceptualisation, methodology, data collection, sample analysis, data analysis, validation, data curation, writing – the initial draft, writing – revisions, project management. F.H.: Conceptualisation, methodology, sample analysis; data analysis, validation, data curation, writing – revisions, student supervision, project leadership, project management. E.S.: Conceptualisation, methodology, sample analysis, data analysis, validation, data curation, writing – revisions, student supervision, project leadership, project management.

References

1. Madamesila J, McGeachy P, Villarreal Barajas JE, Khan R. Characterizing 3D printing in the fabrication of variable density phantoms for quality assurance of radiotherapy. Phys Medica. 2016;32(1):242–247. https://doi.org/10.1016/j.ejmp.2015.09.013
2. Groenewald A, Groenewald WA. Development of a universal medical X-ray imaging phantom prototype. J Appl Clin Med Phys. 2016;17(6):356–365. https://doi.org/10.1120/jacmp.v17i6.6356
3. Ehler ED, Barney BM, Higgins PD, Dusenbery KE. Patient specific 3D printed phantom for IMRT quality assurance. Phys Med Biol. 2014;59(19):5763–5773. https://doi.org/10.1088/0031-9155/59/19/5763
4. Leng S, McGee K, Morris J, Alexander A, Kuhlmann J, Vrieze T, et al. Anatomic modeling using 3D printing: Quality assurance and optimization. 3D Print Med. 2017;3(1), Art. #6. https://doi.org/10.1186/s41205-017-0014-3
5. Chan HK, Griffin J, Lim JJ, Zeng F, Chiu ASF. The impact of 3D printing technology on the supply chain: Manufacturing and legal perspectives. Int J Prod Econ. 2018;205:156–162. https://doi.org/10.1016/j.ijpe.2018.09.009
6. Kapetanakis I, Fountos G, Michail C, Valais I, Kalyvas N. 3D printing X-ray quality control phantoms: A low contrast paradigm. J Phys Conf Ser. 2017;931(1), Art. #012026. https://doi.org/10.1088/1742-6596/931/1/012026
7. Huda W, Abrahams RB. X-ray-based medical imaging and resolution. Am J Roentgenol. 2015;204(4):W393–W397. https://doi.org/10.2214/AJR.14.13126
8. De Crop A. Image quality evaluation in X-ray medical imaging based on Thiel embalmed human cadavers [PhD thesis]. Ghent: Ghent University; 2015. http://hdl.handle.net/1854/LU-8514957
9. Vajuhudeen Z, Jones J. Spatial resolution. Radiopaedia.org. 2009 Jun 05. https://doi.org/10.53347/rID-6318
10. Cohen-Adad J, Wald LL. Chapter 2.1 – Array coils. In: Cohen-Adad J, Wheeler-Kingshott CAM, editors. Quantitative MRI of the spinal cord. Amsterdam: Academic Press; 2014. p. 59–67. https://doi.org/10.1016/B978-0-12-396973-6.00005-8
11. Samei E. Performance of digital radiographic detectors: Quantification and assessment methods. Advances in digital radiography: RSNA Categorical Course in Diagnostic Radiology Physics. Durham, NC: Duke University Medical Center; 2003. p. 37–47.
12. Reis C, Pascoal A, Sakellaris T, Koutalonis M. Quality assurance and quality control in mammography: A review of available guidance worldwide. Insights Imaging. 2013;4(5):539–553. https://doi.org/10.1007/s13244-013-0269-1
13. ISO/PRF 17296-1 – Additive manufacturing – General principles [Internet]. [cited 2021 Dec 03]. Available from: https://standards.iteh.ai/catalog/standards/iso/a31c7a1c-bb3c-4b56-acb9-33e9602e9a2b/iso-prf-17296-1
14. He Y, Liu Y, Dyer BA, Boone JM, Liu S, Chen T, et al. 3D-printed breast phantom for multi-purpose and multi-modality imaging. Quant Imaging Med Surg. 2019;9(1):63–74. https://doi.org/10.21037/qims.2019.01.05
15. Schopphoven S, Cavael P, Bock K, Fiebich M, Mäder U. Breast phantoms for 2D digital mammography with realistic anatomical structures and attenuation characteristics based on clinical images using 3D printing. Phys Med Biol. 2019;64(21):215005. https://doi.org/10.1088/1361-6560/ab3f6a
16. Solomon J, Ba A, Bochud F, Samei E. Comparison of low-contrast detectability between two CT reconstruction algorithms using voxel-based 3D printed textured phantoms. Med Phys. 2016;43(12):6497–6506. https://doi.org/10.1118/1.4967478
17. Lee MY, Han B, Jenkins C, Xing L, Suh TS. A depth-sensing technique on 3D-printed compensator for total body irradiation patient measurement and treatment planning. Med Phys. 2016;43(11):6137. https://doi.org/10.1118/1.4964452
18. Javan R, Bansal M, Tangestanipoor A. A prototype hybrid gypsum-based 3-dimensional printed training model for computed tomography-guided spinal pain management. J Comput Assist Tomogr. 2016;40(4):626–631. https://doi.org/10.1097/RCT.0000000000000415
19. Kamomae T, Shimizu H, Nakaya T, Okudaira K, Aoyama T, Oguchi H, et al. Three-dimensional printer-generated patient-specific phantom for artificial in vivo dosimetry in radiotherapy quality assurance. Phys Med. 2017;44:205–211. https://doi.org/10.1016/j.ejmp.2017.10.005
20. Malliori A, Daskalaki A, Dermitzakis A, Pallikarakis N. Development of physical breast Phantoms for X-ray imaging employing 3D printing techniques. Open Med Imaging J. 2020;12(1):1–10. https://doi.org/10.2174/1874347102012010001
21. Wang S, Pavlicek W, Roberts CC, Langer SG, Zhang M, Hu M, et al. An automated DICOM database capable of arbitrary data mining (including radiation dose indicators) for quality monitoring. J Digit Imaging. 2011;24(2):223–233. https://doi.org/10.1007/s10278-010-9329-y
22. Welvaert M, Rosseel Y. On the definition of signal-to-noise ratio and contrast-to-noise ratio for fMRI data. PLoS One. 2013;8(11):e77089. https://doi.org/10.1371/journal.pone.0077089
23. Bath M. Evaluating imaging systems: Practical applications. Radiat Prot Dosim. 2010;139:26–36. https://doi.org/10.1093/rpd/ncq007